

# A Class D Power Amplifier for Multi-Frequency Eddy Current Testing Based on Multi-Simultaneous-Frequency Selective Harmonic Elimination Pulse Width Modulation

Yang Tao, *Member, IEEE*, Christos Ktistis, Yifei Zhao, Wuliang Yin, *Senior Member, IEEE*, and Anthony J. Peyton

**Abstract**—Efficiency and multisimultaneous-frequency (MSF) output capability are two major criteria characterizing the performance of a power amplifier in the application of multifrequency eddy current testing (MECT). Switch-mode power amplifiers are known to have a very high efficiency, yet they have rarely been adopted in the instrumental development of MECT. In addition, switch-mode power amplifiers themselves are lacking in the research literature for MSF capability. In this article, a Class D power amplifier is designed so as to address the two issues. An MSF selective harmonic elimination pulsewidth modulation method is proposed to generate alternating magnetic fields, which are rich in selected harmonics. A field-programmable-gate-array-based experimental system has been developed to verify the design. Results show that the proposed methodology is capable of generating high MSF currents in the transmitting coil with a low distortion of signal.

**Index Terms**—Class D power amplifier, eddy current, multifrequency, pulsewidth modulation (PWM), selective harmonic elimination.

## I. INTRODUCTION

MULTI-FREQUENCY eddy current testing (MECT) has attracted increasing attention for non-destructive testing (NDT) in recent years. In comparison with the single-frequency eddy current method, MECT takes advantage of wide-band spectral signals, which is advantageous for applications such as detecting cracks in conductive materials [1], measuring thickness of metal film [2], monitoring microstructure in steel production [3] and imaging conductivity profile of metal structures [4], etc. In these applications of MECT, a high-current power amplifier with multi-simultaneous-frequency (MSF) output capability is indispensable in the signal chain so as to achieve high overall sensitivity [5].

Manuscript received March 22, 2019; revised July 17, 2019 and September 2, 2019; accepted October 8, 2019. This work was supported by the U.K. Engineering and Physical Sciences Research Council via the University of Manchester Impact Accelerator Account under Grant EP/R511626/1. (Corresponding author: Yang Tao; Wuliang Yin.)

The authors are with the Department of Electrical and Electronic Engineering, School of Engineering, The University of Manchester, Manchester M13 9PL, U.K. (e-mail: yang.tao@manchester.ac.uk; christos.ktistis@manchester.ac.uk; yifei.zhao@manchester.ac.uk; wuliang.yin@manchester.ac.uk; a.peyton@manchester.ac.uk).

Color versions of one or more of the figures in this article are available online at <http://ieeexplore.ieee.org>.

Digital Object Identifier 10.1109/TIE.2019.2947842

Class D power amplifier has the virtue of high current handling capacity and power efficiency [6], [7]. However, transmitting signals may suffer severe distortion after amplification if they are not modulated properly. A notable category of modulation methods is known as the programmed pulse width modulation (PPWM) or selective harmonic elimination pulse width modulation (SHEPWM) [8] which has drawn tremendous interests and been studied primarily for high-power high-voltage converters [9]. Owing to the lack of motivation of generating multi-simultaneous frequencies using SHEPWM, efforts have been mainly devoted in a manner to achieve varying outputs of the fundamental component which is characterised by the modulation index and to eliminate the remaining harmonics. Yet in MECT applications, the varying modulation index is not of interest while the MSF output capability is of importance. Therefore, some harmonics may be well harnessed rather than eliminated.

This paper attempts, for the first time, to examine the MSF capability of the SHEPWM technique and in addition, to introduce switch-mode power amplifier into the instrumental development of MECT. A Class D power amplifier based upon multi-simultaneous-frequency SHEPWM (MSF-SHEPWM) is designed. The proposed design is capable of driving an excitation coil with a simultaneous multi-frequency signal. Moreover, it is convenient to change the spectrum of the transmitting signal. Experimental results have proved that the system could transmit MSF alternating magnetic fields with low distortion. The remainder of the paper is organised as follows. Section §II describes the principle of MSF-SHEPWM. The design of hardware and the results of experiments are presented in Section §III. Finally, conclusions are drawn in the last section.

## II. MSF-SHEPWM PRINCIPLE

In eddy current testing, the load of the power amplifier is a coil that generates alternating magnetic fields. In order to generate the magnetic fields that are required for MECT, according to the Ampère's law, we can directly design the current through the coil. The waveform of coil current is a concatenation of a few straight line segments of fixed gradients when the coil is connected to a Class D power amplifier. This is due to the fact that in theory the voltage across the coil

can only have a fixed number of values or levels and, for a perfect inductor, the coil current is an integral of the voltage. Figure 1 shows three example topologies for Class D power amplifier. Enhancement-mode n-type MOSFETs are used for this illustration. The components in blue colour constitute a conducting path. Figure 1(a) shows a push-pull configuration where the voltage across the coil have two levels, i.e.  $+V_{DC}/2$  and  $-V_{DC}/2$ ; Figure 1(b) depicts a full H-bridge topology that is capable of driving the coil with three-level voltage, i.e.  $+V_{DC}$ , 0 and  $-V_{DC}$ . Multi-level voltage can be achieved by utilising multiple full H-bridges. For example, a five-level inverter is shown in Figure 1(c) that contains two H-bridge cells. The five values of voltage are  $+2V_{DC}$ ,  $+V_{DC}$ , 0,  $-V_{DC}$  and  $-2V_{DC}$ .

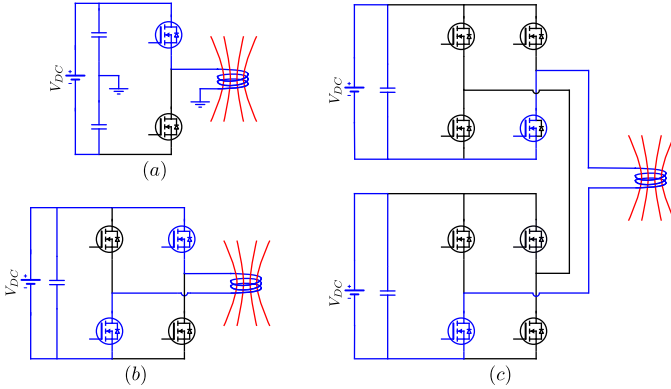


Fig. 1. Topology of Class D power amplifier using enhancement-mode n-type MOSFETs. (a) push-pull half bridge. (b) full H-bridge. (c) two full H-bridges.

The objective of MSF-SHEPWM is to generate an output waveform that contains the desired MSF spectral components, but eliminates the unwanted harmonics. The principle of MSF-SHEPWM can be summarised in three stages. Firstly, the objective signal is synthesised based on the fundamental sinusoidal signal and a few harmonics in the time domain, and the waveform of the synthesised signal is resembled by straight line segments in a morphological sense. Secondly, the resultant resemblance signal is decomposed as Fourier series and analysed in the frequency domain. Finally, the Fourier coefficients are adjusted by solving an optimisation problem. These three stages will now be described in detail in the following sub-sections. For clarity we use  $f_k(t)$  to denote the objective signal,  $g_k(t)$  as the resemblance function of  $f_k(t)$ , and  $G_k(t)$  is the Fourier series of  $g_k(t)$ . The subscript  $k$  refers to a specific signal.

#### A. Synthesis of the objective function $f_k(t)$ in the time domain

A periodic signal  $f(t)$  that contains  $n$  sinusoidal basic components is expressed as (1) where  $\omega_p$ ,  $\theta_p$  and  $w_p$  are the angular frequency, phase angle and coefficient of the  $p^{th}$  component respectively. The function  $f(t)$  serves as the objective coil current that is to be generated and the coefficient  $w_p$  forms the amplitude spectrum.

Additionally, three conditions are exerted on  $f(t)$ . Firstly, the lowest frequency is set as the fundamental frequency  $\omega$

and higher frequencies are harmonics of  $\omega$ , i.e.  $\omega_p = p\omega$ . This is a natural requirement since the signal generated by Class D power amplifier is rich in harmonics. Secondly, the phase angle  $\theta_p$  is zero implying all the basic components are in-phase. In MECT applications, the relative phase values are not critical factors. Thirdly, the coefficient  $w_p$  is chosen as  $\frac{1}{p}$  for the selected frequencies and zero for absent harmonics. In general, the magnitude of response signal tends to increase with frequency. In order to achieve similar signal-to-noise ratio (SNR) in the whole spectrum of interest, the coefficient  $w_p$  is chosen to be inversely proportional to the frequency  $\omega_p$  or the order  $p$ . In fact, (1) is a special case of the trigonometric form of Fourier series but only a few rather than an infinite number of components are involved.

$$f(t) = \sum_{p=1}^n w_p \sin(\omega_p t + \theta_p) \quad (1)$$

$$f_1(t) = \sin(\omega t) + \frac{1}{3} \sin(3\omega t) + \frac{1}{9} \sin(9\omega t) + \frac{1}{27} \sin(27\omega t) + \frac{1}{81} \sin(81\omega t) \quad (2)$$

$$f_2(t) = \sin(\omega t) + \frac{1}{3} \sin(3\omega t) + \frac{1}{7} \sin(7\omega t) + \frac{1}{17} \sin(17\omega t) \quad (3)$$

$$f_3(t) = \sin(\omega t) + \frac{1}{2} \sin(2\omega t) + \frac{1}{4} \sin(4\omega t) + \frac{1}{6} \sin(6\omega t) + \frac{1}{8} \sin(8\omega t) + \frac{1}{10} \sin(10\omega t) + \frac{1}{12} \sin(12\omega t) + \frac{1}{14} \sin(14\omega t) \quad (4)$$

$$f_4(t) = \sin(\omega t) + \frac{1}{2} \sin(2\omega t) + \frac{1}{3} \sin(3\omega t) + \frac{1}{4} \sin(4\omega t) + \frac{1}{5} \sin(5\omega t) + \frac{1}{6} \sin(6\omega t) + \frac{1}{7} \sin(7\omega t) + \frac{1}{8} \sin(8\omega t) \quad (5)$$

$$f_5(t) = \sin(\omega t) + \frac{1}{3} \sin\left(3\omega t + \frac{\pi}{4}\right) + \frac{1}{9} \sin\left(9\omega t + \frac{\pi}{9}\right) + \frac{1}{27} \sin\left(27\omega t + \frac{\pi}{5}\right) + \frac{1}{81} \sin\left(81\omega t + \frac{\pi}{6}\right) \quad (6)$$

As an example, a signal  $f_1(t)$  that follows these principles is shown in Figure 2. Here,  $f_1(t)$  is a superposition of five basic sinusoidal signals. The frequencies are chosen in a geometric scale as  $\omega$ ,  $3\omega$ ,  $9\omega$ ,  $27\omega$  and  $81\omega$ . The weights are set as  $1$ ,  $\frac{1}{3}$ ,  $\frac{1}{9}$ ,  $\frac{1}{27}$ , and  $\frac{1}{81}$ . Another three examples  $f_2(t)$ ,  $f_3(t)$  and  $f_4(t)$  that have different possible combinations of basic components are shown in Figure 3. The expressions of  $f_1(t)$ ,  $f_2(t)$ ,  $f_3(t)$  and  $f_4(t)$  are shown in (2), (3), (4) and (5), respectively.

The selection of involving harmonics has flexibility and is determined by the fundamental frequency and the spectrum

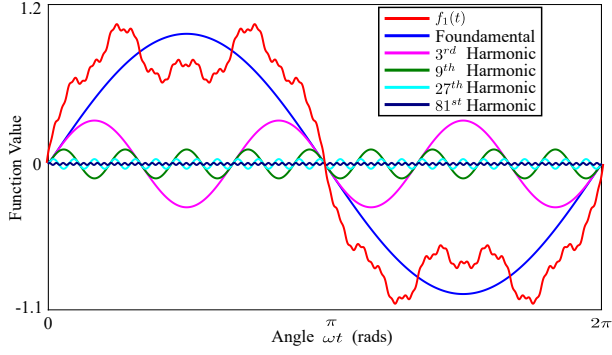


Fig. 2. The objective function  $f_1(t)$ , the corresponding fundamental and harmonic functions

of interest. The associated coefficients are determined by the requirement of power distribution for each harmonics. It should be noted that the basic sinusoidal components do not necessarily have to be in-phase relative to each other. For example,  $f_5(t)$  as expressed in (6), has the same weights for each basic components as  $f_1(t)$ , but the phases are different which is shown in Figure 3. Although  $f_5(t)$  has the same amplitude spectrum as  $f_1(t)$ , some symmetric features are broken which makes the analysis in the frequency domain more complicated.

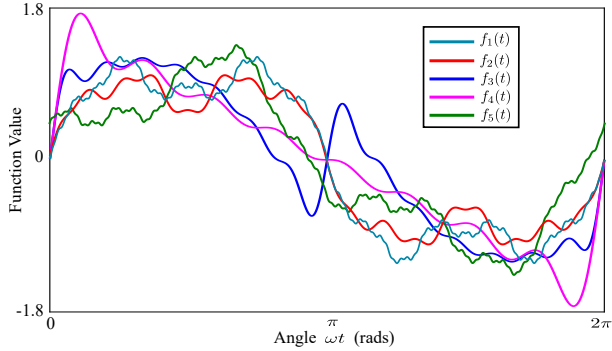


Fig. 3. Objective function:  $f_1(t)$ ,  $f_2(t)$ ,  $f_3(t)$ ,  $f_4(t)$  and  $f_5(t)$

Once the waveform of the objective function is determined, such waveform can be resembled using straight line segments as shown in Figure 4. The resemblance function  $g(t)$  is piecewise linear with different gradients and approximates the objective function  $f(t)$ . Accurate approximation requires multiple levels of output voltage which, however, costs multiple H-bridge cells. Therefore, the selection of voltage levels is a trade-off between the fidelity of signal and feasibility in practice. The number of time steps used for  $g(t)$  is often determined by the clock frequency used to drive the bridge circuit and limited by the dynamic characteristics of the transistor.

### B. Analysis of the resemblance function $g_k(t)$ in the frequency domain

1) *Calculation of the Fourier coefficients for the resemblance function  $g_k(t)$ :* A resemblance function  $g_k(t)$  can be generated by a multi-level Class D power amplifier. The

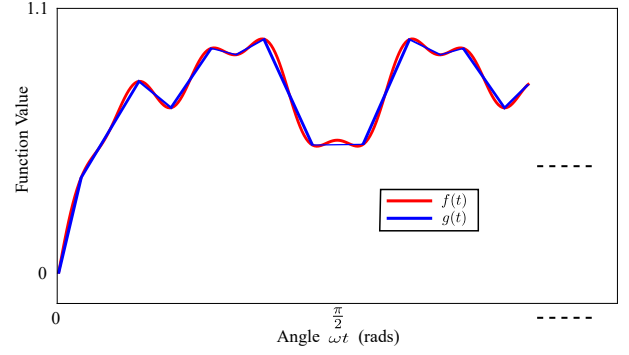


Fig. 4. An objective function  $f(t)$  and its resemblance function  $g(t)$

switching scheme in a quarter period is depicted in Figure 5. Switching angles satisfy  $0 \leq \alpha_1 \leq \alpha_2 \leq \dots \leq \alpha_N \leq \frac{\pi}{2}$  and at each angle the voltage can raise or fall by  $V_0$  until reaching the limits. The coil current is essentially an integral of the pulse voltage which is depicted as the area in the magenta colour in Figure 5. Therefore, the Fourier series of the coil current is calculated as (7). The Fourier coefficient is shown in (8) which is a function of  $N$  switching angles  $\alpha_q$ , the coil inductance  $L$ , the order of harmonics  $p$  and the step of voltage  $V_0$ .

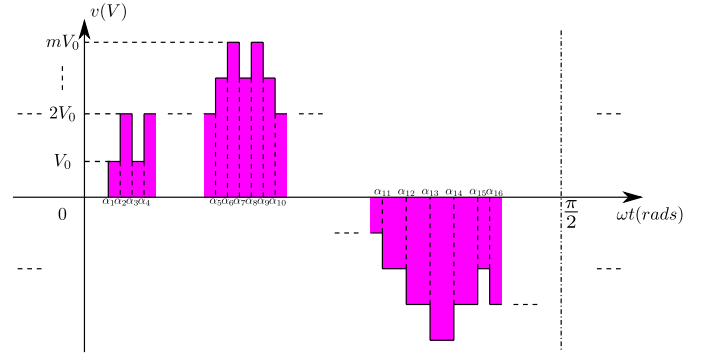


Fig. 5. Switching scheme of multi-level Class D amplifier

$$G(t) = \sum_{p=1,3,\dots}^{\infty} b_p \sin(p\omega t) \quad (7)$$

$$b_p = -\frac{4V_0}{p^2\pi\omega L} \sum_{q=1}^N (-1)^s \sin(p\alpha_q),$$

$$s = \begin{cases} 1 & , \forall \alpha_q \text{ at which there is a falling edge} \\ 0 & , \forall \alpha_q \text{ at which there is a raising edge} \end{cases} \quad (8)$$

### C. Optimisation of the Fourier coefficients $b_p$

Once the waveform of the resemblance function  $g_k(t)$  is obtained based on the gradient of  $f_k(t)$ , the spectrum of  $g_k(t)$  can be controlled by adjusting the switching angles  $\alpha_q$  which is essentially a problem of solving simultaneous transcendental equations. Each equation corresponds to the magnitude of a harmonic to be controlled.

Various methods have been developed in order to obtain one or multiple solutions to the harmonic magnitude equations. One direction for developing a solver is based on the elimination theory of polynomial and using the *resultant* [10]. Unfortunately, the order of polynomials increases with the number of harmonics to be controlled which results in a significant computational burden if the application entails a wide spectrum. Moreover, completely solving the equations might be a stringent requirement and in fact discrepancies could be tolerated within a threshold in a real application. Another direction tends to recast the harmonic magnitude equations into an optimisation problem [8]. Because of the trigonometric and non-convex nature of the harmonic magnitude equations, it is difficult to guarantee that a globally optimal solution can be achieved. Meta-heuristic algorithms such as differential evolution [11], genetic algorithm [12], and particle swarm optimisation [13], etc. have been applied to obtain a global solution through modern stochastic search techniques. However, different results may be returned for the same problem since these algorithms rely on random searches. Many gradient based algorithms, on the other hand, guarantee that a local optimal can be obtained in theory. If a good estimation of the solution exists, the gradient based algorithms could converge to the optimal rapidly [14].

$$\min_{0 \leq \alpha_1 \leq \alpha_2 \leq \dots \leq \alpha_N \leq \frac{\pi}{2}, m_p} \sum_{p \in \Phi} \lambda_p \left( \frac{p\omega L}{V_0} b_p - m_p \right)^2, \\ \text{subject to } \left| \frac{p\omega L}{V_0} b_p \right| \leq \epsilon_p, \forall p \in \Psi \quad (9)$$

In this paper, the harmonic magnitude equations are calculated by solving a constrained nonlinear optimisation problem as shown in (9). Following the convention of multi-level inverter, we denote the modulation index for the  $p^{th}$  harmonic frequency as  $m_p = \frac{V_p}{V_0}$ , where  $V_p$  is the amplitude of the  $p^{th}$  harmonic in the output voltage. The modulation index characterises the relative amplitude of output voltage in the context of a multi-level inverter, but there are two different considerations for MECT. Firstly,  $m_p$  is of interest for multiple harmonics, yet only the fundamental frequency component is relevant for a multi-level inverter. Secondly,  $m_p$  is treated as an optimising parameter, while a multi-level inverter tends to be able to output a range of values of the modulation index. In (9),  $\Phi$  is a set whose elements are the orders of selected harmonics while the elements of  $\Psi$  are the orders of harmonics to be eliminated. The objective function in (9) represents the sum of weighted ( $\lambda_p$ ) squared residuals of the modulation index for selected harmonics subject to such constraints that the modulation index of undesirable harmonics is bounded with threshold  $\epsilon_p$ . The optimising parameters are  $N$  switching angles  $\alpha_1, \alpha_2, \dots, \alpha_N$  and the modulation index  $m_p$ .

The problem (9) could provide many flexibilities in practice. For instance, the adjacent harmonics of an objective frequency will cause interference at that frequency and hence the corresponding threshold  $\epsilon_p$  for the adjacent harmonics should be smaller than those of other less critical harmonics. Additionally, if annulation of the objective function is not

possible, the objective function could be relaxed by putting higher weights  $\lambda_p$  for more important harmonics and lower weights for other harmonics.

The interior-point algorithm is adopted to solve the problem (9). This choice of algorithm is due to the fact that the interior-point algorithm has been proved to be an effective solver for constrained nonlinear optimisation problems [15]. Moreover, both the objective function and constrain function have well-defined Gradient and Hessian. Besides, the initial value of switching angles can be obtained based on the gradient of objective function  $f(t)$  which turns out to be a good estimation. The *MATLAB*<sup>®</sup> *Optimization Toolbox*<sup>®</sup> provides a solver *fmincon* that implements the interior-point algorithm.

### III. HARDWARE AND EXPERIMENTAL RESULTS

#### A. Hardware Implementation

In order to test the proposed MSF-SHEPWM method, an FPGA based experimental system was designed which is shown in Figure 6. The system schematic diagram is shown in Figure 7. The system mainly comprises three parts, namely a *Spartan*<sup>®</sup> – 6 FPGA, power supply and H-bridge circuit. An oscillator on the experiment board generates a clock signal of a fixed frequency, and a digital clock manager (DCM) inside the FPGA is used to generate a specified baseline clock signal for control sequence. The FPGA periodically reads the switching sequence from in-chip memory and outputs pulse signals through a PWM logic block. The pulse signals are then fed into the bridge driver. Four enhancement-mode n-type MOSFETs are utilised in the system configured in a full H-bridge. Therefore, three levels of voltage can be generated by the H-bridge cell. According to the analysis of two cases of application that will be shown in the following paragraphs, even a bipolar pulse voltage is sufficient in generating the desired magnetic fields. Although the proposed MSF-SHEPWM method applies to the design of multiple H-bridge cells, only a single full H-bridge is adopted in the system. In order to make the enhancement-mode n-type MOSFETs working in the ohmic region, the gate-to-source voltage must be higher than not only the threshold voltage, but the addition of the drain-to-source voltage and the threshold voltage. Therefore, a bootstrap circuit is required to drive the high side MOSFETs. The dc voltage is selected as 24 V supplied externally.

#### B. Power and Efficiency Metrics

The drain efficiency  $\eta$  [16] as expressed in (10) is adopted as an efficiency metric, in which the input dc power  $P_{DC}$  is the product of the dc power supply voltage  $V_{DC}$  and current  $I_{DC}$ . The real output power  $P_{out}$  is defined in (11), in which  $u_{out}$ ,  $i_{out}$  and  $T$  are the load voltage, current and integration interval, respectively. As the objective is generating ac magnetic field rather than dissipating dc power in the load, we define an energy conversion factor  $\zeta$  as (12), in which the output reactive power  $Q_{out}$  [17] is defined as (13) where  $U_i$  and  $I_i$  are the root-mean-squared values of the output voltage and current harmonics of order  $i$ .  $\theta_i$  is the phase angle

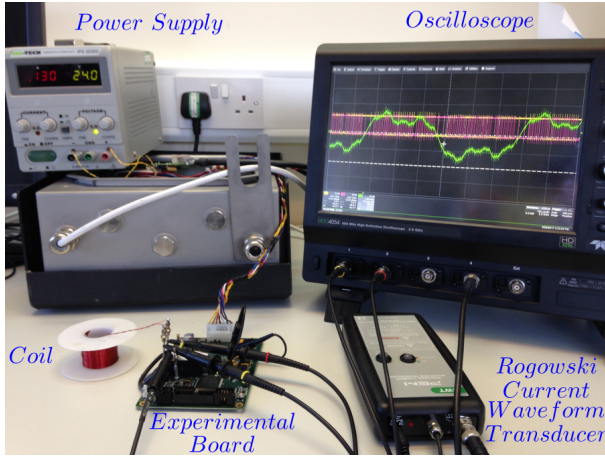


Fig. 6. Experimental system

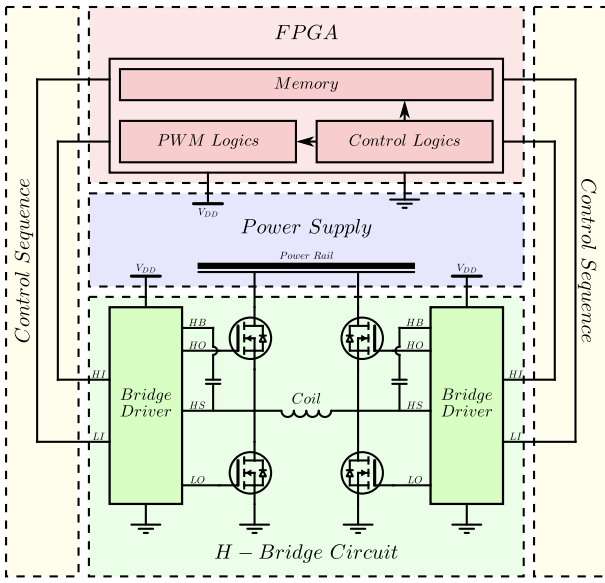


Fig. 7. Schematic diagram of the experimental system

difference between them, and  $\Psi$  is the set containing the orders of transmitting harmonics.

$$\eta = \frac{P_{out}}{P_{DC}} \quad (10)$$

$$P_{out} = \frac{1}{T} \int_T u_{out} i_{out} dt \quad (11)$$

$$\zeta = \frac{Q_{out}}{P_{DC}} \quad (12)$$

$$Q_{out} = \sum_{i \in \Psi} U_i I_i \sin \theta_i \quad (13)$$

### C. Two Experiments

The selection of excitation frequencies is of high importance and it can be expected that different spectrum is required for different applications. For example, the  $\beta$  - dispersion frequency range from hundreds of kilohertz to megahertz is

often harnessed to detect the property which relates to the cellular structure of biological tissues [18], while 20 kHz to 100 kHz is a suitable range for measuring copper film with thickness of 10–400  $\mu m$  [19].

Two experiments are carried out based on the experimental system. In the first experiment, the full design procedures are illustrated and the questions needing attentions are discussed. In the second experiment, we show a fast design without the procedure of analysing in the frequency domain and the optimisation process. The setups of two experiments can be found in Table I.

TABLE I  
DETAILED SETUPS OF TWO EXPERIMENTS

	Experiment No. 1	Experiment No. 2
Selected Harmonics	1 <sup>st</sup> , 3 <sup>rd</sup> , 7 <sup>th</sup> , 17 <sup>th</sup>	1 <sup>st</sup> , 3 <sup>rd</sup> , 9 <sup>th</sup> , 27 <sup>th</sup> , 81 <sup>st</sup>
Clock Frequency	24 MHz	6.25 MHz
Lookup Table Length	476 bits	3888 bits
Transmitting Frequency	50.42 kHz, 151.26 kHz, 352.94 kHz, 857.14 kHz	1.61 kHz, 4.82 kHz, 14.47 kHz, 43.40 kHz, 130.21 kHz
Coil Inductance	1.4 $\mu H$	662 $\mu H$
Wire Diameter (AWG)	13 AWG	26 AWG

1) *Experiment No. 1:* The objective of this experiment is to generate high currents for a low-impedance coil in the frequency range between 10 kHz and 1 MHz. Test samples can be transferred through the aperture of the coil. This configuration could be applied to inline discrimination of metal contaminants, grading of food product and monitoring of meat ageing process, etc.

a) *Excitation frequencies:* Deciding the number of transmitting frequencies is a trade-off between power distribution and spectral resolution. If too many frequencies are selected, it's inevitable that the power will be relatively low for an individual frequency. Moreover, if two selected frequencies are too close, not enough distinction of the response signal could be drawn from them. As a result, four frequencies are chosen for this experiment as the fundamental, 3<sup>rd</sup>, 7<sup>th</sup> and 17<sup>th</sup> harmonics which results in the earlier mentioned objective function  $f_2(t)$  in II-A. The clock frequency is configured as 24 MHz and the highest frequency is  $\frac{1}{28}$  of the clock frequency. Therefore, the four transmitting frequencies are about 50.42 kHz, 151.26 kHz, 352.94 kHz and 857.14 kHz. It is noted that these frequencies well span the objective spectrum but are relatively arbitrary and the transmitting frequencies could be altered by either changing the clock frequency or the ratio of the highest frequency over the clock frequency.

b) *Levels of output voltage:* Determining the number of output voltage levels of the amplifier is another trade-off. As shown in Figure 8, the resemblance function  $g_2(t)$  generated by the bipolar voltage across the coil is able to approximate the objective function  $f_2(t)$  with a tolerable error in practice. It will be justified through practical test that the bipolar output voltage is capable of generating the coil currents with low distortion. In addition, there are only six switching angles  $\alpha_1, \alpha_2, \alpha_3, \alpha_4, \alpha_5$  and  $\alpha_6$  in a quarter period. The highest switching frequency is close to the 17<sup>th</sup> harmonic frequency implying that the magnitude of the harmonic frequencies higher than the highest transmitting frequency will be low. Therefore, a low-pass filter is no longer needed.



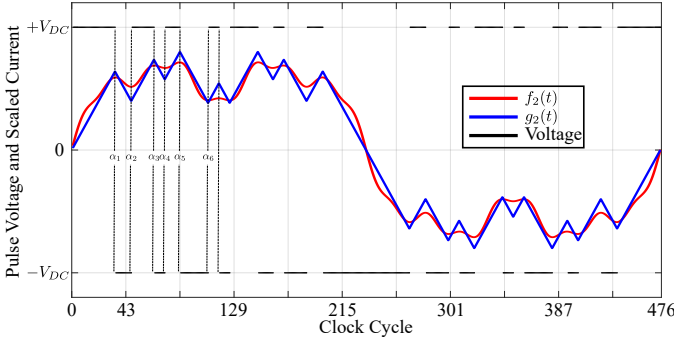


Fig. 8.  $f_2(t)$ ,  $g_2(t)$  and the pulse voltage that generates  $g_2(t)$

c) *Setup of optimisation problem:* According to (8) the Fourier coefficients  $b_p$  of  $g_2(t)$  can be calculated as (14). Cautions should be made that there are two falling edges, i.e.  $+V_{DC}$  to 0 and 0 to  $-V_{DC}$  at  $\alpha_1, \alpha_3, \alpha_5$ , two raising edges, i.e.  $-V_{DC}$  to 0 and 0 to  $+V_{DC}$  at  $\alpha_2, \alpha_4, \alpha_6$ , and one falling edge, i.e.  $+V_{DC}$  to 0 at  $\frac{\pi}{2}$ . Substituting (14) in (9) gives rise to the optimisation problem (15) where the dc voltage  $V_{DC}$  and coil inductance  $L$  have been cancelled. Additionally, because we would like  $b_p$  to be inversely proportional to  $p$ , (15) is in fact normalised where each residual in the objective function should have similar level of magnitude.

$$b_p = -\frac{4V_{DC}}{p^2\pi\omega L} \left( 2 \sum_{q=1}^6 (-1)^q \sin(p\alpha_q) - \sin\left(\frac{p\pi}{2}\right) \right), \quad p = 1, 3, 5, \dots \quad (14)$$

The initial values of the six switching angles are the points where the gradient of  $f_2(t)$  is zero as shown in Figure 8. The angles can only have discrete values and the resolution is determined by the product of the order of the highest harmonic and the ratio of the clock frequency over the highest transmitting frequency. As a result, the length of the lookup table which stores the control sequence is 476 as a product of 17 and 28 and hence the resolution of angle is  $\frac{2\pi}{476}$  rads. Since every switching angle is an integer multiplied by the resolution, it is convenient to use the number of clock cycle to represent the angles. A set of initial values is listed in the first row of Table II. These initial values are substituted into (14) in order to calculate the modulation index  $m_p$ . The objective  $b_p$  of selected harmonics is inversely proportional to  $p$ , so the corresponding modulation index  $m_p$  should have the same value. As a result, the average value of  $m_1, m_3, m_7$  and  $m_{17}$  when substituting the initial angles is used as the initial value for  $m_1, m_3, m_7$  and  $m_{17}$ .

The constrain threshold  $\epsilon_p$  is set up in a way that the scaled modulation index  $\frac{m_p}{p}$  for those undesirable harmonics has the same bound. The modulation index  $m_p$  is scaled by  $p$  because we would like  $b_p$  to have the same bound for undesirable harmonics. All the weights  $\lambda_p$  are configured as one for the first setup and then the residual of the 17<sup>th</sup> harmonic is relaxed by setting  $\lambda_{17}$  as zero which is the second setup. The reason of such relaxation will be discussed in following

paragraphs. Details of the initial condition and two setups for the parameters are listed in Table II.

d) *Results:* The optimisation problem (15) given the initial condition under two setups of parameters is solved using the interior-point algorithm. The resultant switching angles, total harmonic distortion (THD) and scaled modulation index  $\frac{m_p}{p}$  are listed in Table II where the THD is defined as (16). Here we use  $\frac{m_p}{p}$  to represent  $b_p$  because the former is independent of the coil inductance  $L$  while the latter is not. An Fast Fourier Transform (FFT) is conducted to the resemblance functions when the initial switching angles, the optimal angles of the first setup and of the second setup are applied. The results are plotted in Figure 9.

$$THD = \frac{\sqrt{\sum_{p \in \Psi} b_p^2}}{\sqrt{\sum_{p \in \Phi} b_p^2}} \times 100\% \quad (16)$$

It can be seen from Table II that the initial switching angles already lead to a low THD of 7.33 %. However, the power distribution among the four selected frequencies is not the same as desired. The fourth component is higher while the second and third component are lower than they should be. This situation is improved by the optimisation under the first setup. Equal weights are assigned to the four residuals resulting in a more desirable power distribution. However, the THD has been increased to 9.04 % which is mainly caused by the increase of the adjacent harmonic components of 857.14 kHz that can be seen in Figure 9. The reason behind this is that initially the frequency of the highest-frequency ripple is close to 857.14 kHz which in turn gives rise to the large component of 857.14 kHz and a clean spectrum higher than 857.14 kHz. The optimisation process tends to penalise the residual of 857.14 kHz by, unfortunately, increasing its adjacent harmonic components rather than the lower desirable harmonics. Consequently, it is reasonable to always relax the penalty of the 'benign ripple' as has been done in the second setup. As shown in Table II, the scaled modulation index of the first three frequencies have a better ratio comparing to those of the first optimisation while the highest-frequency  $\frac{m_p}{p}$  and THD are similar. The waveforms of the associated resemblance functions for the three sets of switching angles are shown in Figure 10.

The optimal switching angles of the second optimisation setup are implemented in the experimental system to drive a coil with an inductance of about 1.4  $\mu H$ . The screenshot of an oscilloscope displaying the coil current and bipolar output voltage is shown in Figure 11. The peak-to-peak value of the current through the coil is higher than 60 A. An FFT is done to the current and the largest ten root-mean-square (RMS) values and the corresponding frequencies are listed in Table III.

2) *Experiment No. 2:* Compared to the first experiment, the objective of the second experiment is to drive a higher-impedance coil in a lower spectrum from about 1 kHz to 200 kHz. The axis of the coil aperture would point to the test samples. Application of this spectrum can be found in the inspection of welding process, crack detection of metal samples and thickness measurement of metal film, etc.

$$\min_{0 \leq \alpha_1 \leq \alpha_2 \leq \dots \leq \alpha_6 \leq \frac{\pi}{2}, m_p} \sum_{p=1,3,7,17} \lambda_p \left( \frac{8}{p\pi} \sum_{q=1}^6 (-1)^q \sin(p\alpha_q) - \frac{4}{p\pi} \sin\left(\frac{p\pi}{2}\right) + m_p \right)^2,$$

$$\text{subject to } \left| \frac{8}{p\pi} \sum_{q=1}^6 (-1)^q \sin(p\alpha_q) - \frac{4}{p\pi} \sin\left(\frac{p\pi}{2}\right) \right| \leq \epsilon_p, \forall p \in \{5, 9, 11, 13, 15\} \quad (15)$$

TABLE II  
RESIDUAL WEIGHT  $\lambda_p$ , CONSTRAIN THRESHOLD  $\epsilon_p$ , SWITCHING ANGLE  $\alpha_q$ , SCALED MODULATION INDEX  $\frac{m_p}{p}$  AND THE TOTAL HARMONIC DISTORTION FOR THE INITIAL AND TWO OPTIMISATION SETUPS OF EXPERIMENT NO.1

	$\lambda_1$	$\lambda_3$	$\lambda_7$	$\lambda_{17}$	$\epsilon_5$	$\epsilon_9$	$\epsilon_{11}$	$\epsilon_{13}$	$\epsilon_{15}$	Switching angle (clock cycle)						$\frac{m_p}{p}$				THD (%)
										$\alpha_1$	$\alpha_2$	$\alpha_3$	$\alpha_4$	$\alpha_5$	$\alpha_6$	50.42 kHz	151.26 kHz	352.94 kHz	857.14 kHz	
Initial	—	—	—	—	—	—	—	—	—	36	49	68	77	88	111	0.534	0.145	0.066	0.043	7.33
No. 1	1	1	1	1	0.10	0.18	0.22	0.26	0.30	39	51	70	82	90	111	0.553	0.171	0.047	0.032	9.04
No. 2	1	1	1	0	0.10	0.18	0.22	0.26	0.30	35	48	65	74	86	111	0.493	0.157	0.068	0.043	7.80

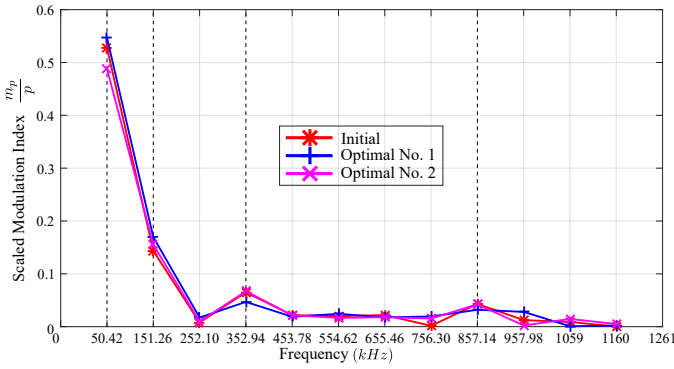


Fig. 9. Scaled modulation index  $\frac{m_p}{p}$  with respect to frequency for the initial switching angles, optimal angles of the first setup and the second setup of experiment No.1

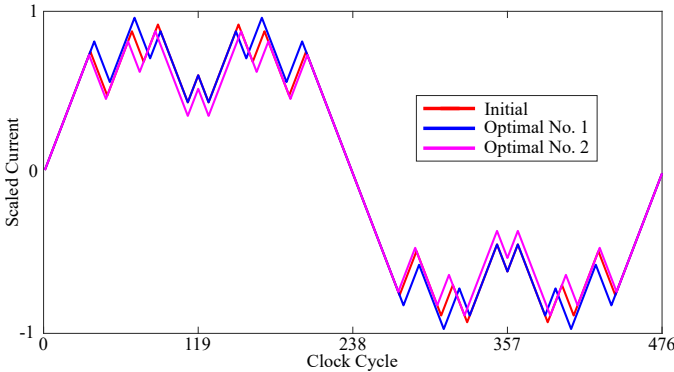


Fig. 10. Waveform of the resemblance function for the initial switching angles, optimal angles of the first setup and the second setup of experiment No.1

The objective function  $f_1(t)$ , as shown in Figure 12, is implemented in this experiment where the fundamental,  $3^{rd}$ ,  $9^{th}$ ,  $27^{th}$  and  $81^{st}$  harmonics are involved. The resemblance function  $g_1(t)$  is also plotted in Figure 12 and there are 38 switching angles in a quarter period of  $g_1(t)$ . Because the highest order harmonic is the  $81^{st}$  harmonic,  $g_1(t)$  requires more switching angles than  $g_2(t)$ . The initial values of the switching angles are determined in the same way as it is in

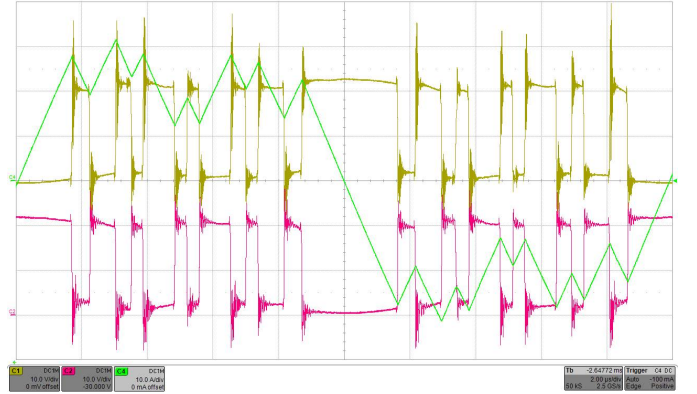


Fig. 11. Coil current (green trace), output voltage of one half bridge (yellow trace) and of the other half bridge (red trace) for optimisation No. 2 of experiment No. 1

TABLE III  
FFT RESULTS OF THE COIL CURRENT FOR OPTIMISATION NO. 2 OF EXPERIMENT NO. 1

No.	Frequency	Current (RMS)	No.	Frequency	Current (RMS)
1	50.42 kHz	16.97 A	6	554.62 kHz	0.76 A
2	151.26 kHz	6.15 A	7	252.10 kHz	0.49 A
3	352.94 kHz	2.08 A	8	1462.18 kHz	0.49 A
4	857.14 kHz	1.49 A	9	756.30 kHz	0.32 A
5	655.46 kHz	0.81 A	10	453.78 kHz	0.31 A

the first experiment, i.e. examining the gradient of objective function. The clock frequency is configured as 6.25 MHz and the five transmitting frequencies are chosen as about 1.61 kHz, 4.82 kHz, 14.47 kHz, 43.40 kHz and 130.21 kHz. As a result, the memory needs 3888 bits to store the control sequence.

In order to show that a fast design could be done without the optimisation process discussed in the first experiment, the initial values of the 38 switching angles are directly implemented in the experimental system. The screenshot of an oscilloscope displaying the coil current and bipolar output voltage is shown in Figure 13. The peak-to-peak value of the current through the coil is about 2.5 A. An FFT is done to the current and the largest ten root-mean-square (RMS) values and

the corresponding frequencies are listed in Table IV.

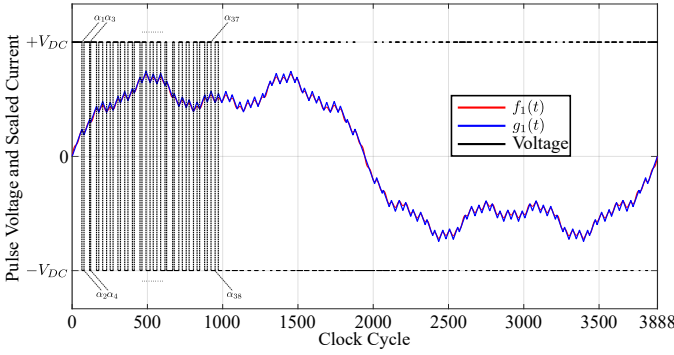


Fig. 12.  $f_1(t)$ ,  $g_1(t)$  and the pulse voltage that generates  $g_1(t)$

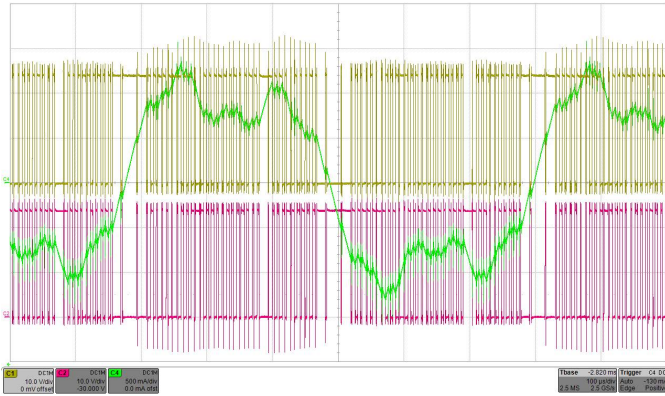


Fig. 13. Coil current (green trace), output voltage of one half bridge (yellow trace) and of the other half bridge (red trace) for experiment No. 2

TABLE IV  
FFT RESULTS OF THE COIL CURRENT FOR EXPERIMENT NO. 2

No.	Frequency	Current (RMS)	No.	Frequency	Current (RMS)
1	1.61 kHz	751.46 mA	6	8.04 kHz	10.53 mA
2	4.82 kHz	284.49 mA	7	20.90 kHz	10.30 mA
3	14.47 kHz	89.05 mA	8	11.25 kHz	7.75 mA
4	43.40 kHz	24.60 mA	9	17.68 kHz	7.52 mA
5	130.21 kHz	22.80 mA	10	27.33 kHz	5.49 mA

3) *Power and efficiency comparison between two experiments:* According to (10), (11), (12) and (13), the power and efficiency metrics of the two experiments are calculated and listed in Table V. In terms of the efficiency  $\eta$ , the first experiment has a lower value of 20.02%, which is due to the fact that the coil has a high quality factor and much of the power is dissipated by the MOSFETs. In contrast, the efficiency  $\eta$  is 76.92% in the second experiment, because the coil is lossy. The energy conversion factor  $\zeta$  is larger than unity for both experiments. The reactive power  $Q_{out}$  for the first experiment is as large as 224.81 var with a total dissipated power of 34.32 W. The second experiment has a lower  $\zeta$  mainly because of its higher impedance of the coil. If possible, we would pursue a low efficiency  $\eta$ , because power dissipation in the load would be a waste of energy. On the other hand, a large energy conversion factor  $\zeta$  is preferred, which implies

that an ac magnetic field would be generated while consuming low dc power.

TABLE V  
POWER AND EFFICIENCY METRICS OF TWO EXPERIMENTS.

Experiment	$V_{DC}$	$I_{DC}$	$P_{DC}$	$P_{out}$	$Q_{out}$	$\eta$	$\zeta$
No. 1	24.00 V	1.43 A	34.32 W	6.87 W	224.81 var	20.02%	6.55
No. 2	24.00 V	0.13 A	3.12 W	2.40 W	8.62 var	76.92%	2.76

## IV. CONCLUSIONS

The instrumental development of MECT entailed a highly efficient amplifier in the transmitting power stage. Switch-mode power amplifiers exhibited compelling advantages in terms of efficiency. This article attempted to serve as a bridge that introduced a switch-mode power amplifier into the design of MECT instrumentation. Being able to transmit MSF magnetic fields was critical in MECT but was not a primary goal in the research of modulation strategy of switch-mode amplifiers or converters. Hence, this article also examined the MSF capability of the SHEPWM technique. A Class D power amplifier was developed in this article aiming at generating high MSF currents in the transmitting coil. An MSF-SHEPWM method was proposed to modulate the pulse voltage across the coil. Three concise steps could summarize the new modulation strategy, i.e., time-domain synthesis of harmonic signals, frequency-domain analysis of the resemblance signal, and optimisation of the resultant Fourier coefficients. An FPGA-based experimental system was developed, and the proposed methodology was implemented in two experiments. The first experiment transmitted magnetic fields exciting at four simultaneous frequencies with a THD as low as 8%. The peak-to-peak value of the coil current was as high as 60A while the total power dissipation was low. The size of the circuit board was small and no large heat dissipating facilities were needed. The second experiment tries to illustrate a fast design process showing that the proposed method was still effective even with the first step only. Five frequencies were transmitted in a smaller span of spectrum comparing to the first experiment. The two experiments have shown that the design is versatile and could be applied to different electromagnetic inductive sensing scenarios.

## ACKNOWLEDGEMENT

All research data supporting this publication are directly available within this publication.

## REFERENCES

- [1] A. Bernieri, G. Betta, L. Ferrigno, and M. Laracca, "Crack Depth Estimation by Using a Multi-Frequency ECT Method," *IEEE Transactions on Instrumentation and Measurement*, vol. 62, no. 3, pp. 544–552, Mar. 2013.
- [2] W. Yin and A. J. Peyton, "Thickness measurement of non-magnetic plates using multi-frequency eddy current sensors," *NDT & E International*, vol. 40, no. 1, pp. 43–48, Jan. 2007.
- [3] S. Johnstone, R. Binns, A. J. Peyton, and W. D. Pritchard, "Using electromagnetic methods to monitor the transformation of steel samples," *Transactions of the Institute of Measurement and Control*, vol. 23, no. 1, pp. 21–29, Mar. 2001.



- [4] W. Yin, S. Dickinson, and A. Peyton, "Imaging the continuous conductivity profile within layered metal structures using inductance spectroscopy," *IEEE Sensors Journal*, vol. 5, no. 2, pp. 161–166, Apr. 2005.
- [5] J. García-Martín, J. Gómez-Gil, and E. Vázquez-Sánchez, "Non-Destructive Techniques Based on Eddy Current Testing," *Sensors*, vol. 11, no. 3, pp. 2525–2565, Feb. 2011.
- [6] J. Rodriguez, J.-S. Lai, and F. Z. Peng, "Multilevel inverters: a survey of topologies, controls, and applications," *IEEE Transactions on Industrial Electronics*, vol. 49, no. 4, pp. 724–738, Aug. 2002.
- [7] M. Malinowski, K. Gopakumar, J. Rodriguez, and M. Pérez, "A Survey on Cascaded Multilevel Inverters," *IEEE Transactions on Industrial Electronics*, vol. 57, no. 7, pp. 2197–2206, Jul. 2010.
- [8] M. S. A. Dahidah, G. Konstantinou, and V. G. Agelidis, "A Review of Multilevel Selective Harmonic Elimination PWM: Formulations, Solving Algorithms, Implementation and Applications," *IEEE Transactions on Power Electronics*, vol. 30, no. 8, pp. 4091–4106, Aug. 2015.
- [9] J. Napoles, J. I. Leon, R. Portillo, L. G. Franquelo, and M. A. Aguirre, "Selective Harmonic Mitigation Technique for High-Power Converters," *IEEE Transactions on Industrial Electronics*, vol. 57, no. 7, pp. 2315–2323, Jul. 2010.
- [10] J. N. Chiasson, L. M. Tolbert, K. J. McKenzie, and Z. Du, "Control of a multilevel converter using resultant theory," *IEEE Transactions on Control Systems Technology*, vol. 11, no. 3, pp. 345–354, May. 2003.
- [11] A. M. Amjad, Z. Salam, and A. M. A. Saif, "Application of differential evolution for cascaded multilevel VSI with harmonics elimination PWM switching," *International Journal of Electrical Power & Energy Systems*, vol. 64, pp. 447–456, Jan. 2015.
- [12] S. S. Lee, B. Chu, N. R. N. Idris, H. H. Goh, and Y. E. Heng, "Switched-Battery Boost-Multilevel Inverter with GA Optimized SHEPWM for Standalone Application," *IEEE Transactions on Industrial Electronics*, vol. 63, no. 4, pp. 2133–2142, Apr. 2016.
- [13] H. Taghizadeh and M. T. Hagh, "Harmonic Elimination of Cascade Multilevel Inverters with Nonequal DC Sources Using Particle Swarm Optimization," *IEEE Transactions on Industrial Electronics*, vol. 57, no. 11, pp. 3678–3684, Nov. 2010.
- [14] S. P. Boyd and L. Vandenberghe, *Convex optimization*. New York: Cambridge University Press, 2004.
- [15] Y. Nesterov and A. Nemirovskii, *Interior-Point Polynomial Algorithms in Convex Programming*, ser. Studies in Applied and Numerical Mathematics. Philadelphia, USA: Society for Industrial and Applied Mathematics, Jan. 1994.
- [16] A. Eroglu, *Introduction to RF Power Amplifier Design and Simulation*. Boca Raton: CRC Press, 2015.
- [17] S. Svensson, "Power measurement techniques for non-sinusoidal conditions," Ph.D. dissertation, Department of Electric Power Engineering, Chalmers University of Technology, 1999.
- [18] M. D. O'Toole, L. A. Marsh, J. L. Davidson, Y. M. Tan, D. W. Armitage, and A. J. Peyton, "Non-contact multi-frequency magnetic induction spectroscopy system for industrial-scale bio-impedance measurement," *Measurement Science and Technology*, vol. 26, no. 3, p. 035102, 2015.
- [19] W. Li, Y. Ye, K. Zhang, and Z. Feng, "A Thickness Measurement System for Metal Films Based on Eddy-Current Method With Phase Detection," *IEEE Transactions on Industrial Electronics*, vol. 64, no. 5, pp. 3940–3949, May. 2017.



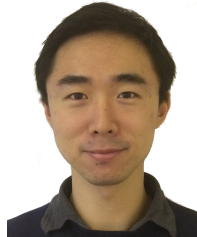
**Yang Tao** (M'19) received the B.Sc. degree in automation and the M.Sc. degree in control science and engineering from Tianjin University, Tianjin, China, in 2010 and 2013, respectively, and the Ph.D. degree in electrical and electronic engineering from the University of Manchester, Manchester, U.K., in 2018.

He is currently a Research Associate with the Department of Electrical and Electronic Engineering, School of Engineering, University of Manchester. His research interests include electromagnetic instrumentation, metal detection, multifrequency power inverter, electromagnetic tomography, inverse problem, sparse representation, and deep learning.



**Christos Ktistis** received the B.Sc. degree in mechanical engineering from the Technological Educational Institution, Serres, Greece, in 2000, the M.Sc. degree in mechatronics from Lancaster University, Lancaster, U.K., in 2002, and the Ph.D. degree in electrical and electronic engineering from The University of Manchester, Manchester, U.K., in 2007.

He is currently a Visitor with the Department of Electrical and Electronic Engineering, School of Engineering, The University of Manchester.



**Yifei Zhao** received the B.Eng. (Hons.) degree and the Ph.D. degree in electrical and electronic engineering from The University of Manchester, Manchester, U.K., in 2010 and 2013, respectively.

He is currently a Visitor with the Department of Electrical and Electronic Engineering, School of Engineering, The University of Manchester.



**Wuliang Yin** (M'05–SM'06) received the B.Sc. and the M.Sc. degrees in electronic measurement and instrumentation from Tianjin University, Tianjin, China, in 1992 and 1995, respectively, and the Ph.D. degree in automotive electronics from Tsinghua University, Beijing, China, in 1999.

He was appointed as a Mettler Toledo (MT) Sponsored Lecturer with the Department of Electrical and Electronic Engineering, School of Engineering, The University of Manchester,

Manchester, U.K., in 2012, and was promoted to a Senior Lecturer in 2016. He has authored 1 book, more than 230 papers, and was granted more than 10 patents in the area of electromagnetic sensing and imaging.

Dr. Yin was a recipient of the 2014 and 2015 Williams Award from the Institute of Materials, Minerals and Mining and the Science and Technology Award from the Chinese Ministry of Education in 2000.



**Anthony J. Peyton** received the B.Sc. degree in electrical engineering and electronics and the Ph.D. degree in medical instrumentation from The University of Manchester Institute of Science and Technology (UMIST), Manchester, U.K., in 1983 and 1986, respectively.

He was appointed as a Principal Engineer with Kratos Analytical Ltd. in 1989, developing precision electronic instrumentation systems for magnetic sector and quadrupole mass spectrometers, from which an interest in electromagnetic instrumentation was developed. He returned to UMIST as a Lecturer and worked with the Process Tomography Group. He moved to Lancaster University in 1996 taking up the post of Senior Lecturer and promoted to a Reader in Electronic Instrumentation in July 2001 and a Professor in May 2004. Since December 2004, he has been a Professor of Electromagnetic Tomography Engineering with the University of Manchester, Manchester. He has been a Principal Investigator of numerous national- and industry-funded projects and a partner of ten previous EU projects, one as a coordinator. He has been a coauthor on almost 140 international journal papers, two books, several hundred conference papers, and 12 patents in areas related to electromagnetics and tomography. His main research interests include instrumentation, applied sensor systems, and electromagnetics.